Growth of highly-oriented (VNbMoTaW)S2 layers

Koichi Tanaka^{†,*}, Hicham Zaid[†], Toshihiro Aoki[§], Aditya Deshpande[†], Koki Hojo[‡], Cristian V. Ciobanu[&] and Suneel Kodambaka^{†,#}

†Department of Materials Science and Engineering, University of California Los Angeles,
410 Westwood plaza, Los Angeles, CA 90095 USA

§Irvine Materials Research Institute (IMRI), University of California Irvine
644 Engineering Tower, Irvine, California 92697, USA

‡Graduate Department of Micro-Nano Mechanical Science and Engineering, Nagoya University,
Furo-cho, Nagoya, Japan

*Department of Mechanical Engineering and Materials Science Program,
Colorado School of Mines, Golden CO 80401, USA

*Department of Materials Science and Engineering,
Virginia Polytechnic Institute and State University, Blacksburg, VA 24061, USA

Abstract

Compositional tunability, an indispensable parameter to modify materials' properties, can open up new applications for the class of van der Waals (vdW) layered materials such as transition-metal dichalcogenides (TMDCs). To-date, multi-element alloy TMDC layers are obtained *via* exfoliation from bulk polycrystalline powders. Here, we demonstrate *direct* deposition of high-entropy alloy disulfide, (VNbMoTaW)S₂, layers with controllable thicknesses on free-standing graphene membranes and on bare and hBN-covered Al₂O₃(0001) substrates *via* ultra-high vacuum reactive dc magnetron sputtering of VNbMoTaW target in Kr and H₂S gas mixtures. Using a combination of density functional theory calculations, Raman spectroscopy, X-ray diffraction, scanning transmission electron microscopy coupled with energy dispersive X-ray spectroscopy, and X-ray photoelectron spectroscopy, we determine that the as-deposited layers are single-phase, 2H-structured, and 0001-oriented (V_{0.10}Nb_{0.16}Mo_{0.19}Ta_{0.28}W_{0.27})S_{2.44}. Our synthesis route is general and applicable for heteroepitaxial growth of a wide variety of TMDC alloys and potentially other multielement alloy vdW compounds with the desired compositions.

Keywords: transition-metal dichalcogenides, multi-element, high-entropy, sputter-deposition, highly-oriented growth

^{*} Corresponding Author: Koichi Tanaka (<u>koichitanaka@uchicago.edu</u>; Present Address: Pritzker School of Molecular Engineering, University of Chicago, Chicago, IL 60637

Transition-metal dichalcogenides (TMDCs) of the general form MX₂, where M is typically a group 4-6 metal and X is one or more of the elements S, Se, and Te, are layered compounds with strong X-M-X covalent and weak out-of-plane van der Waals (vdW) bonding. Among the TMDCs, sulfides such as MoS₂ and WS₂ are probably the most well-studied materials¹ for their applications as catalysts in the petrochemical industry and as dry lubricants in the tribology community.^{2,3} With the emergence of methods to isolate or synthesize atomically-thin crystalline sheets, TMDCs have attracted considerable attention for potential applications in electronics, ⁴ valleytronics, ⁵ and more ⁶ owing to their thickness-dependent properties, which can be metallic or semiconducting depending on the cation and anion chemistries. Probably, the most attractive aspect of TMDCs as twodimensional (2D) layered materials beyond graphene⁷ is that their cation and anion compositions and hence their functionalities can be controlled.⁸⁻¹³ Experimental investigations of TMDC alloys have however largely been limited to two-cation/anion systems with the exception of a few studies on multi-element¹⁴ TMDC alloys. ¹⁵⁻²³. The concept of entropy-stabilized structures composed of an equiatomic alloy of five or more elements has been extended over the past two decades to a variety of compounds (borides, 24 carbides, 25 nitrides, 26, 27 and oxides, 28) including quasi-2D MXenes.^{29, 30} Within the class of 2D TMDCs, alloys with five transition-metals have the highest entropy of mixing (-1.6RT), where R is the universal gas constant) thereby suggesting an entropically stabilized configuration; density functional theory (DFT) calculations^{31, 32} coupled with experiments carried out for selected group 5 and 6 cation compositions revealed that even though some of the ternary alloys are not stable, high-entropy alloy (HEA) TMDCs are stable with superior thermal stability, electrochemical, and electronic characteristics. HEA TMDCs exhibit a variety of properties ¹⁵⁻¹⁷ of interest for applications in energy storage, ¹⁸ energy harvesting (e.g., as piezoelectric¹⁹ and thermoelectric²² materials), in electrocatalysis, ^{20, 21} as mechanical sensors, ¹⁹

and more.^{22, 23} In an effort to discover 2D-layered transition-metal disulfides with new functionalities, Deshpande et al.33 carried out DFT calculations of 126 equi-atomic transitionmetal alloy disulfides each with five out of the nine metals from groups 4, 5, and 6 and predicted that all these compounds are thermodynamically stable at temperatures between 130 and 1200 K. Despite these encouraging reports on HEA TMDC alloys, progress in this area has been limited presumably due to the lack of reliable methods for the growth of multi-element TMDC alloys. Todate, nearly all of the approaches 16, 20, 22 for the synthesis of HEA TMDCs rely on exfoliation of the TMDC layers from polycrystalline bulk samples prepared from alloy powder precursors. The ability to synthesize and assemble in situ TMDC alloy layers of desired composition and layer thickness offers opportunities for substrate-supported vertical assembly of TMDC layers with the desired functionalities for a variety of electronic and optoelectronic applications. Here, we address this issue and demonstrate the growth of highly-oriented HEA TMDC layers on different substrates. Motivated by the recent demonstration of high electrocatalytic activity³¹ of (VNbTaMoW)S₂ and the potential for emerging new properties in the TMDC alloys, given that the parent binary TMDCs, VS₂,³⁴ NbS₂,^{35, 36} TaS₂,³⁷ MoS₂,³⁸ and WS₂,³⁹ exhibit ferromagnetic, metallic, superconducting, and semiconducting characteristics, we choose (VNbTaMoW)S₂ as a model HEA TMDC. In the following sections, we will refer to this compound as HEA-S for brevity.

In this paper, we showcase reactive direct current (dc) magnetron sputtering as an attractive technique for the growth of (VNbMoTaW)S₂ layers, from monolayers up to \sim 15-nm-thick, on bare and hBN-covered Al₂O₃(0001) [hereafter referred to as hBN/Al₂O₃(0001)] substrates and free-standing graphene membranes. Raman spectra obtained from the as-deposited layers reveal two higher intensity peaks at 340.8 cm⁻¹ and 370.0 cm⁻¹, and one lower intensity peak around 288.1 cm⁻¹, which we attribute to E_{2g}^1 and A_{1g}^1 , and E_{1g}^1 vibrations of the HEA-S. Using X-ray

photoelectron (XPS), determine layer spectroscopy we the composition $(V_{0.10}Nb_{0.16}Mo_{0.19}Ta_{0.28}W_{0.27})S_{2.44}$. Cross-sectional transmission electron microscopy (TEM) images show highly layered structure, characteristic of the 2H-structured TMDCs such as MoS₂. In the X-ray diffraction (XRD) 2θ - ω data, we observe multiple high-intensity 000l reflections, indicative of highly 0001-oriented growth, at 20 values corresponding to 2H-phase (P63/mmc) with out-of-plane lattice parameter $c = 1.216 \pm 0.008$ nm. We characterized up to four-layer-thick HEA-S domains directly deposited on free-standing graphene membranes using plan-view TEM, STEM high angle annular dark field (HAADF) imaging, and energy dispersive X-ray spectroscopy (EDS). From the high-resolution plan-view TEM images, we measure in-plane lattice parameter a as 0.32 ± 0.012 nm. The contrast within the STEM images of individual HEA-S domains along with the EDS maps of the elements suggest uniform distribution of transition metals and sulfur across the layer. Our DFT calculations predict that equiatomic (VNbMoTaW)S₂ monolayers are structurally stable and are expected to be metallic.

All the HEA-S layers are grown, following the procedure^{40, 41} described in the Supplementary Information (SI), in a custom-designed UHV system^{42, 43} (base pressure $< 2 \times 10^{-9}$ Torr) on three different types of substrates: 1-to-2 layer thick graphene membranes supported by holey 3-mm-diameter silicon nitride TEM grids (No. 21712, Ted Pella Inc.), $2 \times 10 \times 0.5$ mm³ size Al₂O₃(0001), and hBN/Al₂O₃(0001). The substrate temperatures T_s varied between 1061 and 1349 K (see SI for details). The hBN layers are deposited by pyrolytic cracking of borazine^{44, 45} on Al₂O₃(0001) substrates held at $T_s = 1349$ K following the procedure described elsewhere.^{40, 46} Multilayered HEA-S thin films are deposited by sputtering a nominally equiatomic VNbTaMoW alloy target (99.9% purity, Plasmaterials Inc.) in Kr +H₂S gas discharges with H₂S partial pressure, $p_{H2S} = 0.2$ mTorr. Unless otherwise stated, the total pressure p_{tot} of the gas mixture is set to 5 mTorr. The

deposition times t are 1800 and 1200 s, respectively, for the HEA-S films grown on the Al₂O₃(0001) and hBN/Al₂O₃(0001) substrates. One-to-four-layer thick HEA-S films are obtained by depositing for t = 5, 30, and 60 s directly on the graphene-covered TEM grids at $T_s = 1245$ K, 1126 K, and 1095 K, respectively. The HEA-S thin films on Al₂O₃(0001) and hBN/Al₂O₃(0001) are characterized using one or more of the techniques: XRD, cross-sectional TEM, Raman spectroscopy, and XPS. Higher-resolution imaging and compositional mapping of the HEA-S layers deposited on graphene-covered TEM grids are carried out using plan-view high-resolution TEM, STEM-HAADF, and EDS. Details of the characterization techniques are presented in the SI.

We have carried out DFT calculations of the structure and band structure of the stoichiometric (VNbMoTaW)S₂, and those of the parent sulfides, using the Vienna Ab initio Software Package (VASP),^{47,48} in the framework of the generalized gradient approximation (GGA), with the Perdew, Burke and Ernzerhof (PBE) functional⁴⁹ and the van der Waals functional of Grimme et al.⁵⁰ We use a plane wave energy cutoff of 500 eV and the following k-point grids, depending on the unit cell: 11×11×1 for relaxation and 17×17×1 for density of states (DOS) calculations of the 1×1 parent binary transition-metal disulfide monolayers and 1×1×1 for relaxation and 2×2×1 for the DOS calculations of monolayer 5×5 (VNbMoTaW)S₂. All the structures are fully relaxed (unit cell shape and atomic coordinates) until residual forces are smaller than 0.005 eV/Å; the electronic relaxations at each ionic step are stopped when the energy difference between consecutive self-consistency iterations is 10⁻⁶ eV. The semiconducting or metallic character of the structure was decided based on the location of the Fermi level with respect to the bands in the DOS.

We first present evidence of vdW epitaxial growth of HEA-S on graphene. Figure 1A is a representative high-resolution plan-view TEM image acquired from a few-layer-thick HEA-S

deposited for t = 60 s directly on free-standing graphene membrane supported by holey silicon nitride TEM grid. In the image, we observe lattice fringes, characteristic of crystallinity. The relatively darker contrast features, regular and irregular bands of different widths, visible in the image are likely due to wrinkles in the membrane. One such feature at the top left corner of the image shows six distinct fringes with spacings ranging from 0.57 to 0.61 nm, which we attribute to the presence of five HEA-S layers. Inset in Fig. 1A is a selected area electron diffraction (SAED) pattern, obtained from the same sample but over an area larger than the region seen in A. We find six-fold symmetric set of diffraction spots due to the 0001-oriented graphene membrane, indexed as shown, from which we measure $a = 0.244 \pm 0.001$ nm, the expected value for graphite.⁵¹ The diffraction rings are associated with 0001-oriented, HEA-S layers. Green dashed arcs in the SAED highlight three rings, labeled $\{1\overline{1}00\}$, $\{11\overline{2}0\}$, and $\{2\overline{2}00\}$, that are closest to the central spot. From the ring spacings, we extract $a = 0.32 \pm 0.012$ nm for the HEA-S domains, which is in good agreement with the DFT calculated value of 0.324 nm and is within the range of a values, from 0.315 nm for 2H-WS252 and 0.3420 nm for 1T-NbS2.53 (Please see Table S1 in the SI for a list of all the available lattice parameters of 1T, 2H, and 3R structured MS₂ compounds with M = V, Nb, Ta, Mo, and W.). We suggest below that the HEA-S layers synthesized in our experiments are 2Hstructured compounds, as predicted previously.³³

The fact that we observe diffraction rings rather than spots implies that the HEA-S layers are composed of multiple rotational domains. To determine the orientations and thicknesses of the HEA-S domains within this sample, we divided the TEM image in A into 64 distinct squares, ~8×8 nm² in size, and obtained Fourier transforms (FTs), see Fig. S1. From the spot patterns observed in the FTs, assuming that the lateral sizes of each of the domains is at least 8 nm, we identified regions that are monolayer (1L), bilayer (2L), three-layer (3L), and four-layer (4L) thick, colored

grey, blue, red, and yellow, respectively in Fig. 1B. Fig. S2 shows TEM images acquired from other regions of the sample along with domain thicknesses and their areal coverages. In this sample, grown without optimizing the deposition parameters, we obtain up to four-layer thick domains with relatively larger (38~40%) areal coverages of bilayer and trilayer domains.

In order to determine the structure and composition of the HEA-S layers on graphene, we used STEM and EDS, respectively. Figs. 2A-C are representative, atomic-resolution STEM-HAADF images obtained from 1-2L thick (VNbMoTaW)S_x domains. (Additional STEM-HAADF images acquired from a different HEA-S/graphene sample are shown in Fig. S3.) Within these images, we observe six-fold symmetric arrangement of atoms with different levels of bright and dark contrast. Colored spheres in Figs. 2A and B highlight different stacking sequences seen in these layers. Since STEM-HAADF image intensity is directly related to the atomic number (Z), differences in image contrast could be attributed to differences in Z. Fig. 2D is a plot of image intensities measured as a function of position within the region highlighted using a cyan rectangle in Fig. 2C. (Fig. S3D is a similar plot of image intensities within the yellow rectangle in Fig. S3C.) Based on the overall intensities, we divide the plot into three sections and assign the highest, intermediate, and lowest intensity sections to 2L HEA-S, 1L HEA-S, and graphene membrane, respectively. Within the 1L and 2L HEA-S segments of the plot, we find multiple peaks with at least four different levels of intensities, colored purple, blue, teal, and green, presumably due to four different types of atoms. This is plausible since the Z of transition-metals in the HEA-S vary from 23 for V to 41 for Nb, 42 for Mo, 73 for Ta, and 74 for W. We realize that with the limited resolution of our STEM-HAADF images and in the absence of spatially-resolved EDS or electron energy loss spectra, we cannot accurately relate the peak intensities to the composition of the atoms. Figure 3 shows a representative high-resolution STEM-HAADF image of a HEA-S domain on graphene TEM grid. In this experiment, the HEA-S layer deposition time *t* was 5 s, the shortest time we used with the hope of limiting the HEA-S thickness to a monolayer. We observe contrast variations within the STEM image, likely due to compositional and/or morphological heterogeneities across the domain. Associated panel shows color-coded EDS maps of S, V, W, Nb, Mo, and Ta acquired from the same field of view. (Additional EDS data acquired from a different HEA-S domain is presented in Fig. S4.) All the EDS maps appear to be qualitatively similar, suggestive of spatially-uniform distribution of all the elements.

We now focus on heteroepitaxial growth of HEA-S thin films on bare and hBN-covered Al₂O₃(0001) substrates. Fig. 4A is a typical 2θ - ω XRD scan obtained from HEA-S/Al₂O₃(0001) thin films sputter-deposited using $p_{\rm H_2S} = 2 \times 10^{-4}$ Torr with $p_{\rm tot} = 40$ mTorr at $T_{\rm s} = 1061$ K for t = 1800 s. The peaks labeled s in the plot are due to the single-crystalline Al₂O₃ substrate reflections 0006, and 00012, including the forbidden 0003. We find multiple peaks at $2\theta = 14.71^{\circ}$, 29.37° , 44.60° , 60.68° , and 78.20° , which correspond to interplanar spacings d = 0.6017 nm, 0.3038 nm, 0.2029 nm, 0.1525 nm, and 0.1221 nm, respectively. We attribute all these peaks to 000l reflections of the HEA-S layers, i.e. the HEA-S film is highly 0001-oriented with respect to Al₂O₃(0001), suggestive of heteroepitaxial growth. From the peak positions, we extract an average d value of 0.608 ± 0.004 nm, i.e. $c = 1.216 \pm 0.008$ nm. By comparing the c for our HEA-S film with those in Table S1, we find that it is comparable to and within the range of c for only the 2H-structured parent binary compounds. Figure 4B is a representative cross-sectional TEM image obtained from the same sample. From the image, we measure the film thickness as ~ 23 nm, which corresponds to a deposition rate of 0.013 nm/s. The TEM image reveals smooth surface at the top and layered

structure within the film. FT of the dashed square region, included at the bottom left of the image, shows reflections due to the layered structure of the HEA-S film.

Figures 4C and D are representative Raman spectra and XPS data, respectively from HEA-S thin films deposited on hBN-covered Al₂O₃(0001) following the procedure described in the SI. The red and purple curves in Fig. 4C are Raman spectra obtained, respectively, from HEA-S/hBN/Al₂O₃(0001) and from an HEA-S flake (see Fig. 4C inset) mechanically exfoliated from the Al₂O₃(0001) substrate and transferred onto a Si(100) wafer. We observe two relatively higher intensity peaks at around 340.8 cm⁻¹ and 370.0 cm⁻¹ along with a low-intensity peak around 288.1 cm⁻¹, which we assume correspond to E_{2g}^1 , A_{1g} , and E_{1g} vibrations, respectively, of (VNbMoTaW)S_x. These peaks do not match any of the expected peak positions of the parent binary transition-metal disulfides (see Table S2).

The XPS data in Fig. 4D, from the (VNbMoTaW)S_x/hBN/Al₂O₃(0001) sample, shows multiple peaks associated with all the elements, V, Nb, Ta, Mo, W, and S, as shown in Table 1. We observe S $2p_{1/2}$ and $2p_{3/2}$ peaks at 161.4 eV and 162.7 eV, respectively. All the transition-metal peaks are split into two, one due to sulfide and the other due to oxide phases. Given that our depositions are carried out in O-free atmospheres,^{27, 40} we conclude that the detection of oxide phase in the XPS is likely due to surface oxidation upon air-exposure of the HEA-S sample. Using the intensities of the V $2p_{1/2}$ and $2p_{3/2}$, Nb $3p_{1/2}$ and $3p_{3/2}$, Mo $3p_{1/2}$ and $3p_{3/2}$, Ta $4f_{5/2}$ and $4f_{7/2}$, and W $4p_{3/2}$ peaks associated with the sulfide and the oxide phases, we determine the alloy compositions in the two phases as V_{0.10}Nb_{0.16}Mo_{0.19}Ta_{0.28}W_{0.27} and V_{0.23}Nb_{0.16}Mo_{0.20}Ta_{0.27}W_{0.14}, respectively. Interestingly, we find relatively higher (lower) concentration of V (W) in the oxide than in the sulfide phase, suggestive of preferential oxidation of V. From the S peak intensity together with the metal concentration in only the sulfide phase, we estimate the sulfur-to-metal

ratio as 2.44, i.e. the HEA-S composition is (V_{0.10}Nb_{0.16}Mo_{0.19}Ta_{0.28}W_{0.27})S_{2.44}. Using the cumulative metal peak intensities associated with both the sulfide and the oxide phases, we obtain the sulfur-to-metal ratio as 1.08. We point out that accurate determination of the HEA-S film composition is non-trivial because of incomplete and selective oxidation of the HEA-S film surface coupled with the presence of S and/or metal vacancies. Further investigation, possibly involving the use of *in situ* XPS,⁵⁵⁻⁵⁷ is required for improving our knowledge of the HEA-S composition and its stability against oxidation.

Our DFT calculations predict the existence of a stable HEA-S. We simulated the 1-H structures of the five parent binary transition-metal disulfide and the HEA-S monolayers. (Our calculated lattice parameters for the parent TMDCs are included in Table S1.) Fig. 5A shows simulated structure of an equi-molar and stoichiometric (VNbTaMoW)S₂. The HEA-S monolayer has been simulated as a 5×5 supercell, where the 25 cations of 5 different types are randomly placed in cation sites between the sulfur layers (see Fig. 5A). Fig. 5B is a plot of the DOS for the HEA-S along with the DOS for the five parent binary sulfide monolayers of which two are semiconducting (MoS₂ and WS₂) and three are metallic (NbS₂, TaS₂, and VS₂). For this particular composition of the HEA-S, DFT calculations predict non-zero DOS at the Fermi level, indicative of metallic behavior of the HEA-S.

In conclusion, we report on the direct synthesis and characterization of highly-oriented (VNbMoTaW)S_x layers on free-standing graphene membranes, on hBN-covered Al₂O₃(0001) and on bare Al₂O₃(0001) substrates. Our synthesis approach involves ultra-high vacuum (UHV) sputtering of a high-entropy alloy VNbMoTaW target in a mixture of Kr and H₂S gas discharges. gas atmosphere. We determined the (VNbMoTaW)S_x layer crystallinity and composition using a combination of XRD, S/TEM, EDS, XPS, and Raman spectroscopy. We show that the high-

entropy alloy sulfide is layered, highly 0001-oriented, and isostructural to 2H-MoS₂ with in-plane and out-of-plane lattice parameters of 0.32 ± 0.012 nm and 1.216 ± 0.008 nm, respectively. Raman spectra revealed peaks at 340.8 cm⁻¹, 370.0 cm⁻¹, and around 288.1 cm⁻¹, which we identify as E_{2g}^{1} and A_{1g} , and E_{1g} vibrations of (VNbMoTaW)S_x. Both the lattice parameters and the Raman peaks are within the range of values expected for the parent binary sulfides, XPS data revealed the presence of both metal-S and metal-O bonds for all the five transition-metals, indicative of oxidation of the sulfide, likely occurring upon air-exposure after deposition. From the XPS peak intensities, we obtain the sulfur-to-metal ratio as 2.44 with transition-metal alloy contents as $V_{0.10}Nb_{0.16}Mo_{0.19}Ta_{0.28}W_{0.27}$ and $V_{0.23}Nb_{0.16}Mo_{0.20}Ta_{0.27}W_{0.14}$, respectively, in the sulfide and the oxide phases, suggestive of selective oxidation of V and resistance to oxidation of W. Twodimensional EDS maps obtained from few-layer-thick (VNbMoTaW)S_x domains sputterdeposited directly on free-standing graphene sheets suggest uniform distribution of the transitionmetals and the sulfur in the layers. Our results are consistent with the DFT calculations,³³ which predict the lowest formation enthalpy for this equiatomic combination of transition metals. Experimental validation of the thermodynamic stability of these HEA-S layers may require annealing at elevated temperatures ($T > T_s$) for prolonged times both in vacuum and in the presence of S. Such studies, preferably conducted in situ while monitoring the film composition and structure will likely yield new insights into the thermal stability of this class of materials.

These studies leveraged our prior experience^{40, 41} with reactive dc magnetron sputter-deposition of one of the parent sulfides, MoS₂, heteroepitaxially on Al₂O₃(0001) and hBN/Al₂O₃(0001). Similar approach can be used to grow other binary and multi-element sulfides. While we have demonstrated highly-oriented growths, additional studies are required to optimize the deposition parameters to yield layers with precisely controlled thicknesses and S-

concentration. Finally, the sputter-deposition method presented here can be used to grow single-crystalline thin films⁵⁸ and modified to using elemental metal or binary sulfide targets, rather than the HEA target, to facilitate tunability of the alloy composition and hence maybe more attractive than conventional chemical vapor transport for the synthesis of multi-element alloy TMDCs. With the recent advances in machine learning capabilities, high throughput computations have increasingly been used to explore wide compositional space and to discover new materials with novel or superior properties. We expect that our synthesis approach is capable of depositing monolithic and heterolayered vdW and conventional 3D materials with the desired composition, crystallinity, and thickness, and hence is likely to experimentally validate the computationally predicted compositions.

Supporting Information (SI)

The Supporting Information is available free of charge at [URL].

Additional TEM data of the (VNbMoTaW) S_x layers and schematics of (VNbMoTaW) S_x domains on graphene (PDF)

Author Contributions

S.K. and K.T. conceived the research. K.T. conducted borazine depositions. K.T., H.Z., K.H., and A.D., synthesized and characterized sputter-deposited samples. C.V.C. performed DFT calculations. S.K. managed the project. S.K., K.T., and C.V.C wrote the paper with contributions from all the authors. All authors discussed the results and analysis.

Notes

The authors declare no competing financial interest.

Acknowledgments

We acknowledge the support from the Air Force Office of Scientific Research (AFOSR, Dr. Ali Sayir) Grant Nos. FA9550-18-1-0050 and FA9550-20-1-0184. S.K. acknowledges the National Science Foundation (NSF) for DMR Award No. 2211350 (Dr. James Edgar). K.T. was supported by the Japanese Student Service Organization (L16111111026) and the UCLA Department of Materials Science and Engineering (MSE). A.D. was partially supported by UCLA MSE. K.H. was supported by the Japan U.S. Advanced Collaborative Education Program (JUACEP). The authors acknowledge the use of facilities and instrumentation at the UC Irvine Materials Research Institute (IMRI), which is supported in part by the NSF through the UC Irvine Materials Research Science and Engineering Center (DMR-2011967). We thank Mr. Noah Bodzin and the Nanoelectronics Research Facility in the UCLA Henry Samueli School of Engineering for assistance with focused ion beam milling and acknowledge the use of instruments at the Electron Imaging Center for NanoMachines supported by NIH (1S10RR23057) and the California NanoSystems Institute at UCLA.

References

- 1. Chianelli, R. R.; Berhault, G.; Torres, B. Unsupported transition metal sulfide catalysts: 100 years of science and application. *Catalysis Today* **2009**, 147 (3), 275-286.
- 2. Vazirisereshk, M. R.; Martini, A.; Strubbe, D. A.; Baykara, M. Z. Solid Lubrication with MoS2: A Review. *Lubricants* **2019**, 7 (7).
- 3. Muratore, C.; Voevodin, A. A. Chameleon Coatings: Adaptive Surfaces to Reduce Friction and Wear in Extreme Environments. *Ann. Rev. Mater. Res.* **2009**, 39, 297-324.
- 4. Wang, Q. H.; Kalantar-Zadeh, K.; Kis, A.; Coleman, J. N.; Strano, M. S. Electronics and optoelectronics of two-dimensional transition metal dichalcogenides. *Nature Nanotechnology* **2012**, 7 (11), 699-712.
- 5. Xiao, D.; Liu, G. B.; Feng, W.; Xu, X.; Yao, W. Coupled spin and valley physics in monolayers of MoS2 and other group-VI dichalcogenides. *Phys Rev Lett* **2012**, 108 (19), 196802.
- 6. Cazalilla, M. A.; Ochoa, H.; Guinea, F. Quantum spin Hall effect in two-dimensional crystals of transition-metal dichalcogenides. *Phys Rev Lett* **2014**, 113 (7), 077201.
- 7. Butler, S. Z.; Hollen, S. M.; Cao, L. Y.; Cui, Y.; Gupta, J. A.; Gutierrez, H. R.; Heinz, T. F.; Hong, S. S.; Huang, J. X.; Ismach, A. F.; Johnston-Halperin, E.; Kuno, M.; Plashnitsa, V. V.; Robinson, R. D.; Ruoff, R. S.; Salahuddin, S.; Shan, J.; Shi, L.; Spencer, M. G.; Terrones, M.; Windl, W.; Goldberger, J. E. Progress, Challenges, and Opportunities in Two-Dimensional Materials Beyond Graphene. *ACS Nano* **2013**, 7 (4), 2898-2926.
- 8. Kobayashi, Y.; Mori, S.; Maniwa, Y.; Miyata, Y. Bandgap-tunable lateral and vertical heterostructures based on monolayer Mo1-x W x S2 alloys. *Nano Research* **2015**, 8 (10), 3261-3271.
- 9. Zhang, W.; Li, X.; Jiang, T.; Song, J.; Lin, Y.; Zhu, L.; Xu, X. CVD synthesis of Mo((1-x))W(x)S2 and MoS(2(1-x))Se(2x) alloy monolayers aimed at tuning the bandgap of molybdenum disulfide. *Nanoscale* **2015**, 7 (32), 13554-60.
- 10. Dong, L.; Lou, J.; Shenoy, V. B. Large In-Plane and Vertical Piezoelectricity in Janus Transition Metal Dichalchogenides. *ACS Nano* **2017**, 11 (8), 8242-8248.
- 11. Yanase, T.; Watanabe, S.; Uehara, F.; Weng, M.; Nagahama, T.; Shimada, T. Synthesis of $Mo_{1-x}Nb_xS_2$ thin films by separate-flow chemical vapor deposition with chloride sources. *Thin Solid Films* **2018**, 649, 171-176.
- 12. Dong, J.; Zhao, Y.; Ouyang, G. The effect of alloying on the band engineering of two-dimensional transition metal dichalcogenides. *Physica E: Low-dimensional Systems and Nanostructures* **2019**, 105, 90-96.

- 13. Hemmat, Z.; Cavin, J.; Ahmadiparidari, A.; Ruckel, A.; Rastegar, S.; Misal, S. N.; Majidi, L.; Kumar, K.; Wang, S.; Guo, J.; Dawood, R.; Lagunas, F.; Parajuli, P.; Ngo, A. T.; Curtiss, L. A.; Cho, S. B.; Cabana, J.; Klie, R. F.; Mishra, R.; Salehi-Khojin, A. Quasi-Binary Transition Metal Dichalcogenide Alloys: Thermodynamic Stability Prediction, Scalable Synthesis, and Application. *Adv Mater* **2020**, 32 (26), e1907041.
- 14. Susarla, S.; Kutana, A.; Hachtel, J. A.; Kochat, V.; Apte, A.; Vajtai, R.; Idrobo, J. C.; Yakobson, B. I.; Tiwary, C. S.; Ajayan, P. M. Quaternary 2D Transition Metal Dichalcogenides (TMDs) with Tunable Bandgap. *Advanced Materials* **2017**, 29 (35), 1702457.
- 15. Ying, T.; Yu, T.; Qi, Y.; Chen, X.; Hosono, H. High Entropy van der Waals Materials. *Advanced Science* **2022**, 9 (30), 2203219.
- 16. Ying, T.; Yu, T.; Shiah, Y.-S.; Li, C.; Li, J.; Qi, Y.; Hosono, H. High-Entropy van der Waals Materials Formed from Mixed Metal Dichalcogenides, Halides, and Phosphorus Trisulfides. *Journal of the American Chemical Society* **2021**, 143 (18), 7042-7049.
- 17. Chen, H.; Li, S.; Huang, S.; Ma, L.; Liu, S.; Tang, F.; Fang, Y.; Dai, P. High-entropy structure design in layered transition metal dichalcogenides. *Acta Mater.* **2022**, 222, 117438.
- 18. Cheng, W.; Liu, J.; Hu, J.; Peng, W.; Niu, G.; Li, J.; Cheng, Y.; Feng, X.; Fang, L.; Wang, M.-S.; Redfern, S. A. T.; Tang, M.; Wang, G.; Gou, H. Pressure-Stabilized High-Entropy (FeCoNiCuRu)S2 Sulfide Anode toward Simultaneously Fast and Durable Lithium/Sodium Ion Storage. *Small* **2023**, 19 (29), 2301915.
- 19. Chen, Y.; Tian, Z.; Wang, X.; Ran, N.; Wang, C.; Cui, A.; Lu, H.; Zhang, M.; Xue, Z.; Mei, Y.; Chu, P. K.; Liu, J.; Hu, Z.; Di, Z. 2D Transition Metal Dichalcogenide with Increased Entropy for Piezoelectric Electronics. *Advanced Materials* **2022**, 34 (48), 2201630.
- 20. Qu, J.; Elgendy, A.; Cai, R.; Buckingham, M. A.; Papaderakis, A. A.; de Latour, H.; Hazeldine, K.; Whitehead, G. F. S.; Alam, F.; Smith, C. T.; Binks, D. J.; Walton, A.; Skelton, J. M.; Dryfe, R. A. W.; Haigh, S. J.; Lewis, D. J. A Low-Temperature Synthetic Route Toward a High-Entropy 2D Hexernary Transition Metal Dichalcogenide for Hydrogen Evolution Electrocatalysis. *Advanced Science* **2023**, 10 (14), 2204488.
- 21. Wu, L.; Hofmann, J. P. High-entropy transition metal chalcogenides as electrocatalysts for renewable energy conversion. *Current Opinion in Electrochemistry* **2022**, 34, 101010.
- 22. Buckingham, M. A.; Ward-O'Brien, B.; Xiao, W.; Li, Y.; Qu, J.; Lewis, D. J. High entropy metal chalcogenides: synthesis, properties, applications and future directions. *Chemical Communications* **2022**, 58 (58), 8025-8037.
- 23. Nemani, S. K.; Torkamanzadeh, M.; Wyatt, B. C.; Presser, V.; Anasori, B. Functional two-dimensional high-entropy materials. *Communications Materials* **2023**, 4 (1), 16.
- 24. Gild, J.; Zhang, Y.; Harrington, T.; Jiang, S.; Hu, T.; Quinn, M. C.; Mellor, W. M.; Zhou, N.; Vecchio, K.; Luo, J. High-Entropy Metal Diborides: A New Class of High-Entropy Materials and a New Type of Ultrahigh Temperature Ceramics. *Scientific Reports* **2016**, 6 (1), 37946.

- 25. Harrington, T. J.; Gild, J.; Sarker, P.; Toher, C.; Rost, C. M.; Dippo, O. F.; McElfresh, C.; Kaufmann, K.; Marin, E.; Borowski, L.; Hopkins, P. E.; Luo, J.; Curtarolo, S.; Brenner, D. W.; Vecchio, K. S. Phase stability and mechanical properties of novel high entropy transition metal carbides. *Acta Mater.* **2019**, 166, 271-280.
- 26. Zaid, H.; Tanaka, K.; Ciobanu, C. V.; Yang, J.-M.; Kodambaka, S.; Kindlund, H. Growth of elastically-stiff, nanostructured, high-entropy alloy nitride, (VNbTaMoW)N/Al2O3(0001) thin film. *Scr. Mater.* **2021,** 197.
- 27. Zaid, H.; Tanaka, K.; Liao, M.; Goorsky, M. S.; Kodambaka, S.; Kindlund, H. Self-Organized Growth of 111-Oriented (VNbTaMoW)N Nanorods on MgO(001). *Nano Lett.* **2021**, 21 (1), 577-582.
- 28. Rost, C. M.; Sachet, E.; Borman, T.; Moballegh, A.; Dickey, E. C.; Hou, D.; Jones, J. L.; Curtarolo, S.; Maria, J.-P. Entropy-stabilized oxides. *Nature Communications* **2015**, 6 (1), 8485.
- 29. Nemani, S. K.; Zhang, B.; Wyatt, B. C.; Hood, Z. D.; Manna, S.; Khaledialidusti, R.; Hong, W.; Sternberg, M. G.; Sankaranarayanan, S. K. R. S.; Anasori, B. High-Entropy 2D Carbide MXenes: TiVNbMoC3 and TiVCrMoC3. *ACS Nano* **2021**, 15 (8), 12815-12825.
- 30. Zhou, J.; Tao, Q.; Ahmed, B.; Palisaitis, J.; Persson, I.; Halim, J.; Barsoum, M. W.; Persson, P. O. Å.; Rosen, J. High-Entropy Laminate Metal Carbide (MAX Phase) and Its Two-Dimensional Derivative MXene. *Chem. Mat.* **2022**, 34 (5), 2098-2106.
- 31. Cavin, J.; Ahmadiparidari, A.; Majidi, L.; Thind, A. S.; Misal, S. N.; Prajapati, A.; Hemmat, Z.; Rastegar, S.; Beukelman, A.; Singh, M. R.; Unocic, K. A.; Salehi-Khojin, A.; Mishra, R. 2D High-Entropy Transition Metal Dichalcogenides for Carbon Dioxide Electrocatalysis. *Adv Mater* **2021**, 33 (31), e2100347.
- 32. Hemmat, Z.; Cavin, J.; Ahmadiparidari, A.; Ruckel, A.; Rastegar, S.; Misal, S. N.; Majidi, L.; Kumar, K.; Wang, S.; Guo, J.; Dawood, R.; Lagunas, F.; Parajuli, P.; Ngo, A. T.; Curtiss, L. A.; Cho, S. B.; Cabana, J.; Klie, R. F.; Mishra, R.; Salehi-Khojin, A. Quasi-Binary Transition Metal Dichalcogenide Alloys: Thermodynamic Stability Prediction, Scalable Synthesis, and Application. *Advanced Materials* **2020**, 32 (26), 1907041.
- 33. Deshpande, A.; Ratsch, C.; Ciobanu, C. V.; Kodambaka, S. Entropy stabilization of two-dimensional transition metal dichalcogenide alloys: A density functional theory study. *Journal of Applied Physics* **2022**, 131 (23), 234302.
- 34. Fuh, H. R.; Chang, C. R.; Wang, Y. K.; Evans, R. F.; Chantrell, R. W.; Jeng, H. T. Newtype single-layer magnetic semiconductor in transition-metal dichalcogenides VX2 (X = S, Se and Te). *Sci Rep* **2016**, 6, 32625.
- 35. Guillamon, I.; Suderow, H.; Vieira, S.; Cario, L.; Diener, P.; Rodiere, P. Superconducting density of states and vortex cores of 2H-NbS2. *Phys Rev Lett* **2008**, 101 (16), 166407.

- 36. Zhao, S.; Hotta, T.; Koretsune, T.; Watanabe, K.; Taniguchi, T.; Sugawara, K.; Takahashi, T.; Shinohara, H.; Kitaura, R. Two-dimensional metallic NbS2: growth, optical identification and transport properties. *2D Materials* **2016**, 3 (2).
- 37. Navarro-Moratalla, E.; Island, J. O.; Manas-Valero, S.; Pinilla-Cienfuegos, E.; Castellanos-Gomez, A.; Quereda, J.; Rubio-Bollinger, G.; Chirolli, L.; Silva-Guillen, J. A.; Agrait, N.; Steele, G. A.; Guinea, F.; van der Zant, H. S.; Coronado, E. Enhanced superconductivity in atomically thin TaS₂. *Nat Commun* **2016**, 7, 11043.
- 38. Ganatra, R.; Zhang, Q. Few-Layer MoS2: A Promising Layered Semiconductor. *ACS Nano* **2014**, 8 (5), 4074-4099.
- 39. Ovchinnikov, D.; Allain, A.; Huang, Y.-S.; Dumcenco, D.; Kis, A. Electrical Transport Properties of Single-Layer WS2. *ACS Nano* **2014**, 8 (8), 8174-8181.
- 40. Deshpande, A.; Hojo, K.; Tanaka, K.; Arias, P.; Zaid, H.; Liao, M.; Goorsky, M.; Kodambaka, S. K. hBN-Layer-Promoted Heteroepitaxy in Reactively Sputter-Deposited MoSx≈2(0001)/Al2O3(0001) Thin Films: Implications for Nanoelectronics. *ACS Applied Nano Materials* **2023**, 6 (4), 2908-2916.
- 41. Deshpande, A.; Hojo, K.; Tanaka, K.; Arias, P.; Zaid, H.; Liao, M.; Goorsky, M.; Kodambaka, S. Need for complementary techniques for reliable characterization of MoS2-like layers. *Journal of Vacuum Science & Technology A* **2023**, 41 (4).
- 42. Tanaka, K.; Aleman, A.; Liao, M. E.; Wang, Y.; Goorsky, M. S.; Kodambaka, S. Effects of ultra-low ethylene partial pressure on microstructure and composition of reactively sputter-deposited Ta–C thin films. *Thin Solid Films* **2019**, 688, 137440.
- 43. Tanaka, K.; Fankhauser, J.; Zaid, H.; Aleman, A.; Sato, M.; Yu, D.; Ebnonnasir, A.; Li, C.; Kobashi, M.; Goorsky, M. S.; Kodambaka, S. Kinetics of Zr-Al intermetallic compound formation during ultra-high vacuum magnetron sputter-deposition of Zr/Al2O3(0001) thin films. *Acta Mater.* **2018**, 152, 34-40.
- 44. Arias, P.; Abdulslam, A.; Ebnonnasir, A.; Ciobanu, C. V.; Kodambaka, S. Bifurcation and orientation-dependence of corrugation of 2D hexagonal boron nitride on palladium. *2D Materials* **2018**, 5 (4).
- 45. Arias, P.; Ebnonnasir, A.; Ciobanu, C. V.; Kodambaka, S. Growth Kinetics of Two-Dimensional Hexagonal Boron Nitride Layers on Pd(111). *Nano Lett.* **2020**, 20 (4), 2886-2891.
- 46. Tanaka, K.; Arias, P.; Hojo, K.; Watanabe, T.; Liao, M. E.; Aleman, A.; Zaid, H.; Goorsky, M. S.; Kodambaka, S. K. Borazine Promoted Growth of Highly Oriented Thin Films. *Nano Lett.* **2023**, 23 (10), 4304-4310.
- 47. Kresse, G.; Furthmuller, J. Efficiency of ab-initio total energy calculations for metals and semiconductors using a plane-wave basis set. *Comput. Mater. Sci.* **1996**, 6 (1), 15-50.

- 48. Kresse, G.; Furthmuller, J. Efficient iterative schemes for ab initio total-energy calculations using a plane-wave basis set. *Physical Review B* **1996**, 54 (16), 11169-11186.
- 49. Perdew, J. P.; Burke, K.; Ernzerhof, M. Generalized Gradient Approximation Made Simple. *Physical Review Letters* **1996,** 77 (18), 3865-3868.
- 50. Grimme, S.; Antony, J.; Ehrlich, S.; Krieg, H. A consistent and accurate ab initio parametrization of density functional dispersion correction (DFT-D) for the 94 elements H-Pu. *J Chem Phys* **2010**, 132 (15), 154104.
- 51. Wirtz, L.; Rubio, A. The phonon dispersion of graphite revisited. *Solid State Communications* **2004**, 131 (3), 141-152.
- 52. Schutte, W. J.; De Boer, J. L.; Jellinek, F. Crystal structures of tungsten disulfide and diselenide. *J. Solid State Chem.* **1987,** 70 (2), 207-209.
- 53. Carmalt, C. J.; Manning, T. D.; Parkin, I. P.; Peters, E. S.; Hector, A. L. Formation of a new (1T) trigonal NbS2 polytype via atmospheric pressure chemical vapour deposition. *Journal of Materials Chemistry* **2004**, 14 (3).
- 54. Tanaka, K.; Aleman, A.; Zaid, H.; Liao, M. E.; Hojo, K.; Wang, Y.; Goorsky, M. S.; Kodambaka, S. Ultra-high vacuum dc magnetron sputter-deposition of 0001-textured trigonal α-Ta2C/Al2O3(0001) thin films. *Materialia* **2020**, 13.
- 55. Greczynski, G.; Kindlund, H.; Petrov, I.; Greene, J.; Hultman, L. Sputter-cleaned Epitaxial VxMo(1-x)Ny/MgO(001) Thin Films Analyzed by X-ray Photoelectron Spectroscopy: 1. Single-crystal V0.48Mo0.52N0.64. *Surface Science Spectra* **2013**, 20 (1), 68-73.
- 56. Greczynski, G.; Kindlund, H.; Petrov, I.; Greene, J.; Hultman, L. Sputter-cleaned Epitaxial VxMo(1-x)Ny/MgO(001) Thin Films Analyzed by X-ray Photoelectron Spectroscopy: 2. Single-crystal V0.47Mo0.53N0.92. *Surface Science Spectra* **2013**, 20 (1), 74-79.
- 57. Greczynski, G.; Kindlund, H.; Petrov, I.; Greene, J.; Hultman, L. Sputter-cleaned Epitaxial VxMo(1-x)Ny/MgO(001) Thin Films Analyzed by X-ray Photoelectron Spectroscopy: 3. Polycrystalline V0.49Mo0.51N1.02. *Surface Science Spectra* **2013**, 20 (1), 80-85.
- 58. Aleman, A.; Li, C.; Zaid, H.; Kindlund, H.; Fankhauser, J.; Prikhodko, S. V.; Goorsky, M. S.; Kodambaka, S. Ultrahigh vacuum dc magnetron sputter-deposition of epitaxial Pd(111)/Al2O3(0001) thin films. *Journal of Vacuum Science & Technology A: Vacuum, Surfaces, and Films* **2018,** 36 (3), 030602.

Figures and Tables

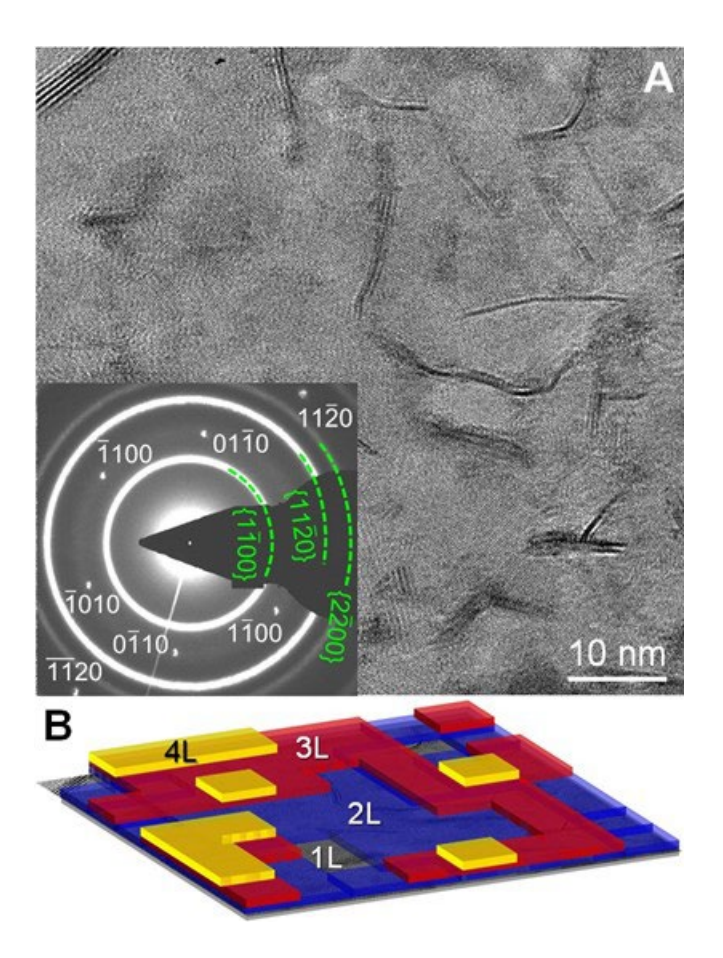


Figure 1. (color online) (**A**) Plan-view bright field transmission electron microscopy (TEM) image of a few-layer-thick HEA-S on free-standing graphene membrane. The thin regular and irregular bands visible in the image are wrinkles in the membrane. (inset) Selected area electron diffraction (SAED) pattern acquired from the same sample but over a region larger than that in **A**. Diffraction spots, indexed as shown, are due to the graphene layers. Diffraction rings, highlighted by green dashed arcs, are due to 2H-structured, 0001-oriented HEA-S layers. (**B**) Perspective view showing areal coverages of monolayer, bilayer, 3-layer, and 4-layer domains in **A**, colored grey, blue, red, and yellow, respectively. Fourier transforms (FTs) (see Fig. S1) from $\sim 8\times 8$ nm² square areas in **A** are used to determine the relative orientations and thicknesses of the domains. In this sample, the HEA-S layers are reactively sputter-deposited in 5 mTorr Kr+H₂S gas mixture with $p_{\text{H2S}} = 0.2$ mTorr on a graphene-covered holey silicon nitride TEM grid at $T_{\text{s}} = 1098$ K for t = 60 s.

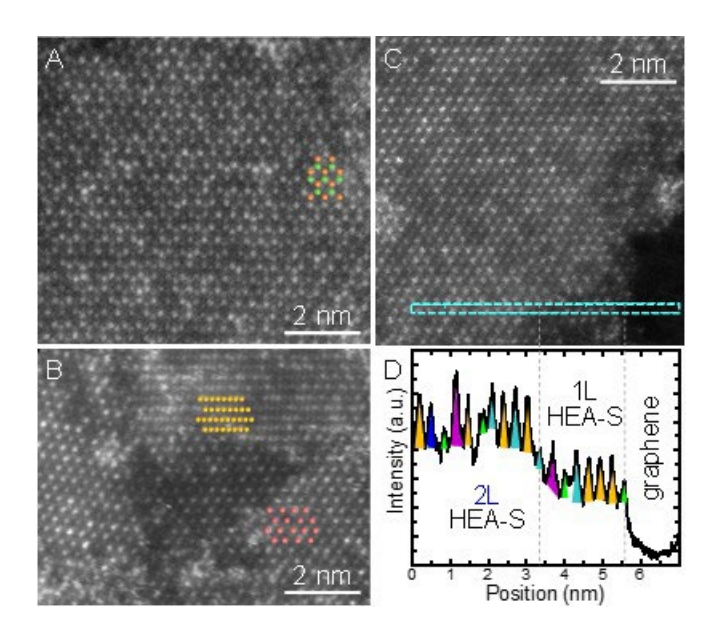


Figure 2. (color online) (**A-C**) Representative STEM images of 1-2 layer HEA-S domains on graphene acquired with a high angle annular dark field detector (HAADF). Colored spheres in **A** and **B** represent TM atoms arranged in different stacking sequences. (**D**) Line profile of image intensity measured along dashed cyan rectangle in **C**. The intensity data is an average of intensities within the rectangle width of 0.245 nm. Colors within the peaks highlight different intensity levels. In this sample, the HEA-S layers are reactively sputter-deposited using 5 mTorr Kr+H₂S gas mixture with $p_{\text{H2S}} = 0.2$ mTorr on a graphene-covered holey silicon nitride TEM grid at $T_{\text{s}} = 1126$ K for t = 30 s.

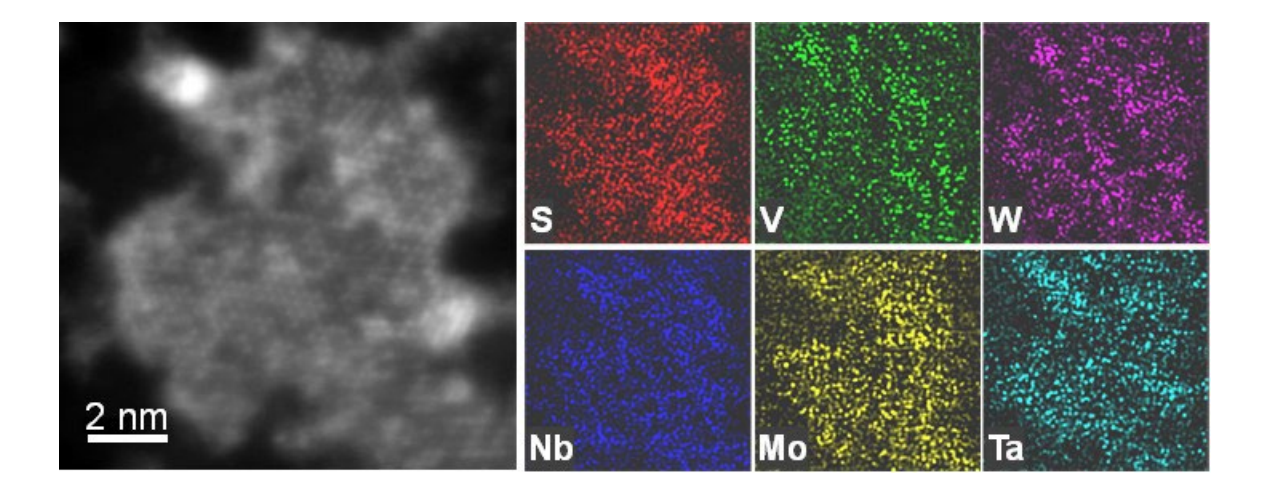


Figure 3. (color online) Representative STEM-HAADF image of a (VNbMoTaW)S_x domain on a graphene-covered TEM grid sputter-deposited at $T_s = 1245$ K for t = 5 s in 5 mTorr Kr+H₂S gas mixture with $p_{\rm H2S} = 0.2$ mTorr. Associated panels show energy dispersive spectroscopy (EDS) signal intensity maps of S K, V K, W L, Nb L, Mo L, and Ta L lines obtained from the same field of view as in the STEM image.

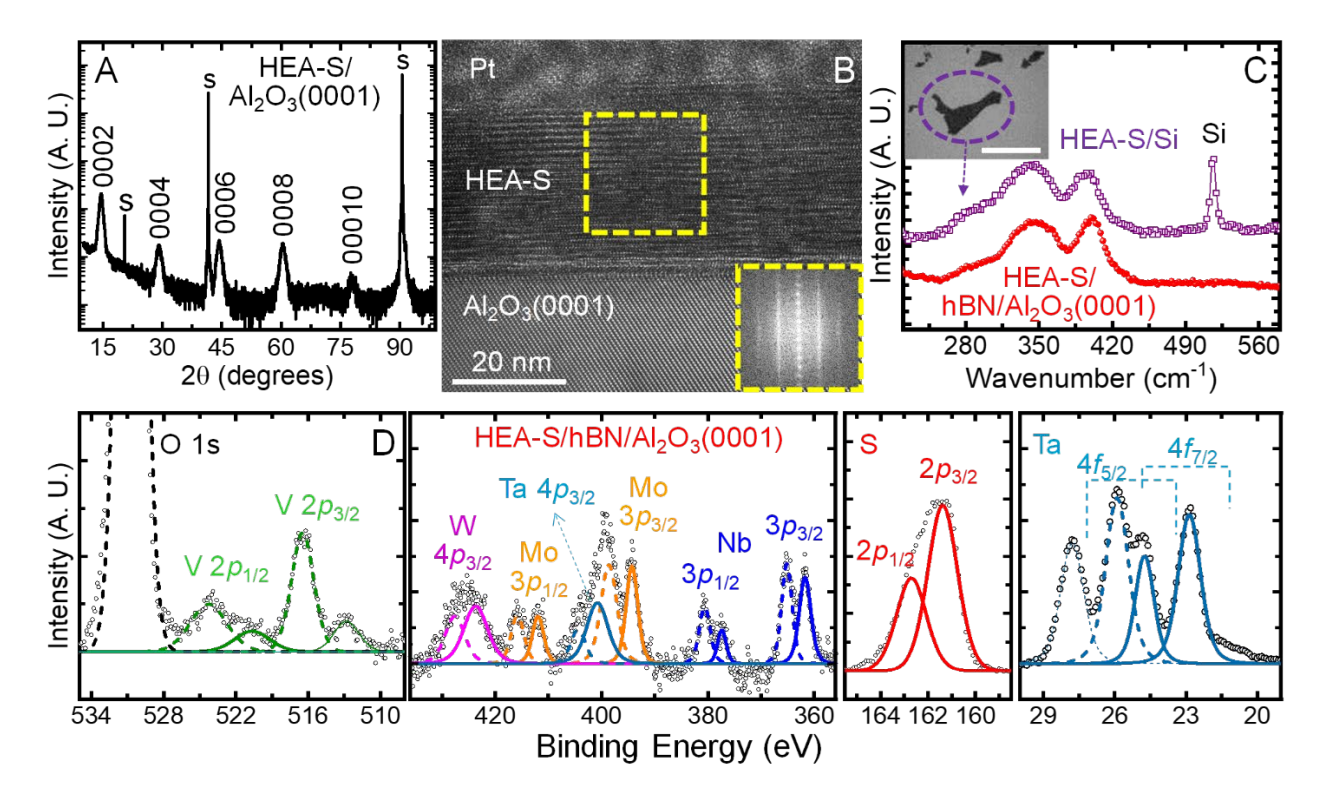


Figure 4. (color online) (**A**) Typical 2θ-ω X-ray diffraction (XRD) scan obtained from an HEA-S/Al₂O₃(0001) thin film. The peaks labeled **s** denote Al₂O₃ 0003, 0006, and 00012 reflections at progressively higher 2θ values. HEA-S peaks are indexed as shown. (**B**) Representative cross-sectional TEM image acquired from the same sample as in **A**. (**C**) Representative Raman spectra obtained, using a 488 nm laser, from (red) the as-deposited HEA-S thin film on hBN/Al₂O₃(0001) and (purple) a mechanically transferred flake of HEA-S on Si(100) wafer. The peak labeled Si is from the Si(100) substrate. (Inset) Optical microscope image (scale bar is 40 μm) of the HEA-S flakes transferred on Si(100). (**D**) X-ray photoelectron spectroscopy (XPS) data (open symbols) acquired from the same HEA-S/hBN/Al₂O₃(0001) sample as in **C**. Solid and dashed lines are Gaussian fits to metal-S and metal-O peaks, respectively of: (magenta) W 4*p*_{3/2}; (orange) Mo 3*p*_{3/2} and 3*p*_{1/2}; (teal) Ta 4*p*_{3/2}, 4*f*_{5/2}, and 4*f*_{7/2}; (blue) Nb 3*p*_{3/2} and Nb 3*p*_{1/2}; (green) V 2*p*_{3/2} and V 2*p*_{1/2}; (red) S 2*p*_{3/2} and 2*p*_{1/2}; and (black) O 1s. The HEA-S layers on Al₂O₃(0001) [hBN/Al₂O₃(0001)] are sputter-deposited at $T_s = 1061$ K [1349 K] for t = 1800 s [1200 s] in Kr+H₂S gas mixtures, $p_{tot} = 4 \times 10^{-2}$ Torr [5 × 10⁻³ Torr], with $p_{H2S} = 2 \times 10^{-4}$ Torr.

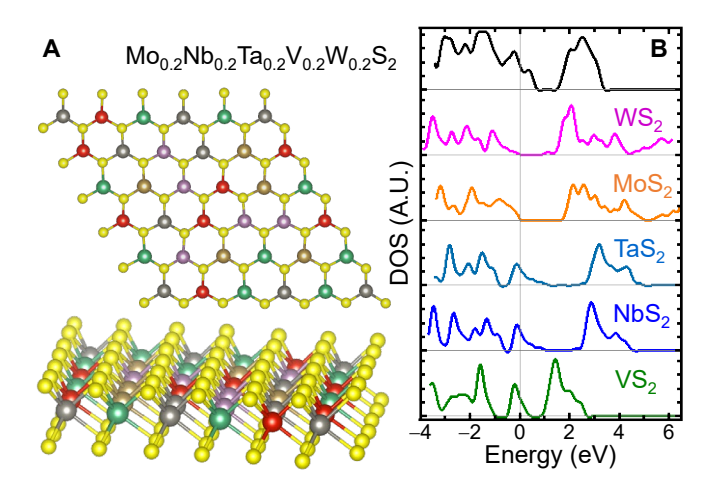


Figure 5. (A) Simulated structure and (B) density of states (DOS) of a monolayer (VNbTaMoW) S_2 with equi-molar cations and stoichiometric sulfur. At this composition, the DOS is non-zero at the Fermi level, i.e. the HEA-S is metallic. For comparison, DOS for the parent binary sulfides, MoS₂, NbS₂, TaS₂, VS₂, and WS₂ are included in the plot.

 $\label{eq:Table 1. Peak positions of XPS spectral line peaks in Fig. 4D, obtained from the HEA-S thin film grown on $hBN/Al_2O_3(0001)$.}$

Element	Spectral Line	Binding Energy / eV	
		Sulfide	Oxide
V	$2p_{1/2}$	520.7	524.3
	$2p_{3/2}$	512.8	516.5
Nb	$3p_{1/2}$	377.4	380.6
	$3p_{3/2}$	361.7	365.2
Mo	$3p_{1/2}$	412.0	415.8
	$3p_{3/2}$	394.3	398.6
Ta	$4p_{3/2}$	400.3	404.2
	$4f_{5/2}$	22.9	25.9
	$4f_{7/2}$	24.7	27.8
W	$4p_{3/2}$	424.1	427.9
S	$2p_{1/2}$	161.4	-
	$2p_{3/2}$	162.7	-